Journal of Alloys and Compounds 506 (2010) 841–848

Contents lists available at ScienceDirect

Journal of Alloys and Compounds

journal homepage: www.elsevier.com/locate/jallcom

The correlation of C14/C15 phase abundance and electrochemical properties in the AB_2 alloys

K. Young[a,*], T. Ouchi[a], B. Huang[a], B. Chao[a], M.A. Fetcenko[a], L.A. Bendersky[b], K. Wang[c], C. Chiu[b]

[a] Energy Conversion Devices Inc./Ovonic Battery Company, 2983 Waterview Drive, Rochester Hills, MI 48309, USA
[b] Materials Science & Engineering Laboratory, NIST, Gaithersburg, MD 20899, USA
[c] Metallurgy Division, NIST, Gaithersburg, MD 20899, USA

ARTICLE INFO

Article history:
Received 7 June 2010
Received in revised form 8 July 2010
Accepted 9 July 2010
Available online 16 July 2010

Keywords:
Hydrogen absorbing materials
Transition metal alloys
Metal hydride electrode
Electrochemical reactions

ABSTRACT

The C14/C15 phase abundance is an important parameter in the design of a suitable AB_2-based metal hydride electrode for use in nickel metal hydride batteries. In order to separate the contribution due to chemical composition from that of phase abundance, three multi-phase and multi-element AB_2 alloys with different C14/C15 phase abundances before and after annealing were studied by scanning electron microscope, transmission electron microscope, X-ray diffraction, pressure-concentration isotherm, half-cell, and full-cell measurements. After annealing at 800 °C for 14 h, the C14 phase abundances increased from 71 to 94% for the first alloy ($Ti_{12}Zr_{21.5}V_{10}Ni_{40.2}Co_{1.5}Cr_{8.5}Mn_{5.6}Al_{0.4}Sn_{0.3}$), remained unchanged at about 50% for the second alloy ($Ti_{12}Zr_{21.5}V_{10}Ni_{40.2}Co_{5.0}Cr_{5.5}Mn_{5.1}Al_{0.4}Sn_{0.3}$), and decreased from 32 to 7% for the third alloy ($Ti_{12}Zr_{21.5}V_{10}Ni_{40.2}Co_{8.0}Cr_{3.5}Mn_{4.1}Al_{0.4}Sn_{0.3}$). The effect of reduction in the amount of non-Laves Zr_xNi_y secondary phases by annealing was established with the second alloy while the contribution of additional major phase (either C14 or C15) by annealing can be distilled by comparing various properties between samples before and after annealing. After the comparison, C15 structure was found to have a higher hydrogen storage capacity and higher reversibility in gas phase hydrogen storage, and better high-rate dischargeability, hydrogen bulk diffusion, specific power, and low temperature performance with a shortcoming of an inferior cycle life in electrochemistry. Results from gas phase hydrogen storage measurement also agree with those from electrochemical testing. Besides, the non-Laves Zr_xNi_y secondary phases are found to play importance roles in the reversibility of hydrogen storage in the gas phase and battery performance in activation, rate capability, charge retention, and cycle life.

1. Introduction

Recently, the AB_2 alloys have been studied extensively for the metal hydride electrode in the nickel metal hydride (Ni/MH) battery application [1–10]. The main storage phases for AB_2 alloys here are two Laves phases, namely C14 with a hexagonal structure and C15 with a face-center-cubic structure [11–24]. Although the structures and stabilities of these two Laves phases were discussed in great detail in the two-part publication by Stein et al. [25,26], there were only a few direct comparisons of the hydrogen storage and electrochemical characteristic of C14 vs. C15 phases [27–31]. All of these comparisons were based on varying the compositions to alter the phase abundances and therefore the contribution of composition cannot be eliminated from the conclusion [29–31]. For example, Song et al. reported the electrochemical comparison results from a series of $ZrMn_{0.9-x}V_xNi_{1.1}$ (x from 0.1 to 0.8) alloys and concluded that C15 phase with stacking faults enhanced the activation and high-rate dischargeability (HRD) of the electrode [27,28]. However, in his case, alloys with high C15 phase contents were also high in Mn in place of V. Mn is known to facilitate the activation and destabilize the metal hydride [32,33]. Consequently, the assertion of easier activation and better HRD performance of C15 phase is less reliable. Moreover, counter argument of C14 carrying better HRD can also be found in the comparison studies [30,34,35]. Therefore, a comparison of the hydrogen storage and electrochemical properties between C14 and C15 structures with similar (if not exactly the same) chemical compositions becomes essential to the further improvement in the performance of AB_2 electrode for Ni/MH battery application.

Rapid-quench [36–45] and annealing ([33,41,46–59] are two common methods to alter the constituent phase abundances in Laves phase and/or other non-Laves minor phases in AB_2 alloys without changing the overall chemical composition. The drawback of rapid-quench is the possibility of producing microcrystalline and even amorphous components, which increases the complexity of comparison [41,44]. The annealing process is not perfect either since it will reduce the abundances of the non-Laves phases, such as Zr_7Ni_{10} [50] or Zr_9Ni_{11}. In this case, the syner-

---

[*] Corresponding author. Tel.: +1 248 293 7000; fax: +1 248 299 4520.
E-mail address: kwoyoung@yahoo.com (K. Young).

0925-8388/$ – see front matter © 2010 Elsevier B.V. All rights reserved.
doi:10.1016/j.jallcom.2010.07.091

getic effect between the Laves phases and the secondary phases has to be taken into consideration in the interpretation of the comparison results.

2. Experimental setup

Two melting methods were used to prepare the ingot samples. Samples from arc melting and induction melting of similar AB_2 alloys were compared before and the conclusion was the difference is very minor and does not affect the structural, thermo dynamical, and electrochemical properties of the alloys [60]. For preparing structural analysis samples, arc melting was performed under flowing argon with a non-consumable tungsten electrode and a water-cooled copper tray. Before each arc melt, a piece of sacrificial titanium underwent a melting–cooling cycle a few times to reduce the residual oxygen concentration. Each 10-g ingot was re-melted and turned over a few times to ensure uniformity in the chemical composition. For preparing samples for sealed cell study, induction melting was performed under an argon atmosphere in a 2 kg induction melting furnace using a $MgAl_2O_4$ crucible, an alumina tundish, and a steel pancake-shape mold. The annealing of ingots was done in a vacuum furnace with diffusion pump and mechanical pump reaching a base pressure of 1×10^{-8} Torr. The annealing condition was 2-h ramp-up to 800 °C, hold at 800 °C for 14 h, and followed by natural cooling in vacuum (about 10 h to room temperature). The chemical composition of each sample was examined by a Varian *Liberty* 100 inductively coupled plasma (ICP) system. A Philips *X'Pert Pro* X-ray diffractometer (XRD) was used to study the microstructure, and a JOEL-*JSM6320F* scanning electron microscopy (SEM) with energy dispersive spectroscopy (EDS) capability was used to study the phase distribution and composition. Elemental microanalysis was carried out with a Bruker “Quad SDD” silicon drift detector energy dispersive X-ray spectrometer (SDD-EDS) mounted on a JEOL8500F thermal field emission electron probe microanalyzer/SEM. Pressure–concentration–temperature (PCT) characteristics for each sample were measured using a Suzuki-Shokan multi-channel PCT system. In the PCT analysis, each sample was first activated by a 2-h thermal cycle between 300 °C and room temperature at 25 atm H_2 pressure. Then PCT isotherms at 30 °C were measured. Details of both electrode and cell preparations as well as measurement methods have been reported before [60,61].

3. Results and discussion

Three AB_2 compositions were selected for this study, #177($Ti_{12}Zr_{21.5}V_{10}Ni_{40.2}Co_{1.5}Cr_{8.5}Mn_{5.6}Al_{0.4}Sn_{0.3}$), #190($Ti_{12}Zr_{21.5}V_{10}Ni_{40.2}Co_{5.0}Cr_{5.5}Mn_{5.1}Al_{0.4}Sn_{0.3}$), and #193($Ti_{12}Zr_{21.5}V_{10}Ni_{40.2}Co_{8.0}Cr_{3.5}Mn_{4.1}Al_{0.4}Sn_{0.3}$). While compositions of other elements were kept constant, amounts of Co, Cr, and Mn were varied to cover a range of average electron density (e/a), which is known to affect the C14 and C15 phase abundance ratio [11,52,62–65]. Based on experience, the C14/C15 threshold of e/a is between 6.9 [66] and 7.1 [64] for this family of AB_2 alloys suitable as metal hydride (MH) electrode. Three compositions in this study were designed to be C14-rich (#177, $e/a = 6.91$), C14/C15-equal (#190, $e/a = 7.01$), and C15-rich (#193, $e/a = 7.09$) before annealing.

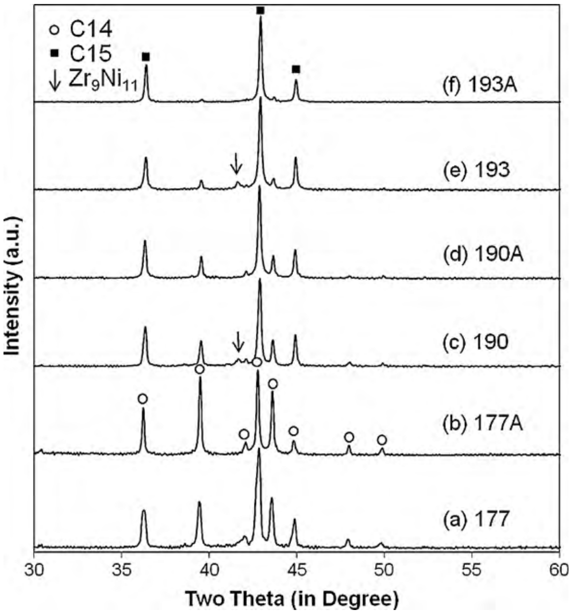

Fig. 1. XRD spectra using Cu-K_α as the radiation source for alloys #177 before (a) and after annealing (b), #190 before (c) and after annealing (d), and #193 before (e) and after annealing (f).

3.1. XRD phase analysis

The XRD spectra of three as-received (#177, #190 and #193) and three annealed samples (#177A, #190A, and #193A) are plotted in Fig. 1. The main components for these alloys are C14 and

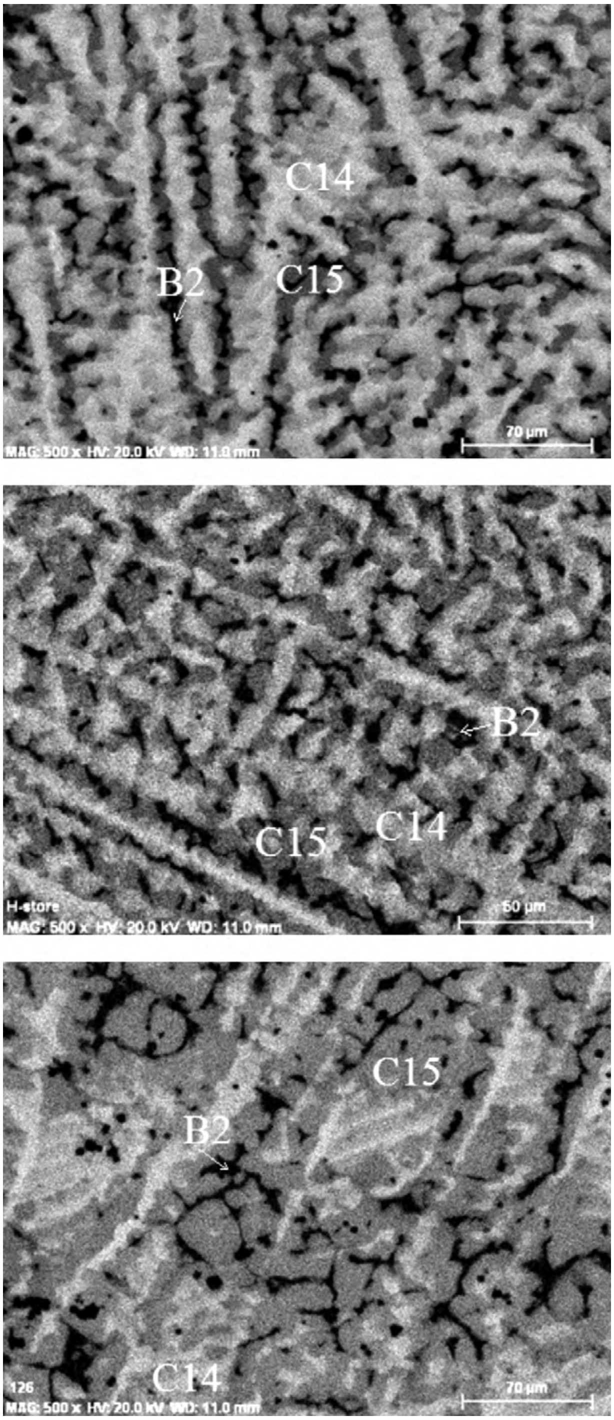

Fig. 2. EDS Cr-mappings for as-prepared #177 (a), #190 (b), and #193 (c). The bright, gray, and dark regions in the micrographs are C14, C15, and interdendritic B2 phases, respectively.

C15 with small amount of Zr_9Ni_{11} secondary phases before annealing. Phase abundances were calculated by Rietveld method and are listed in Table 2. Both pattern factor (R_p) and weighted pattern factor (R_{wp}) are less than 3.5% indicating good curve fitting. The results of predominance of C14 phase for alloy #177 and C15 phase for alloy #193 follow the design. After annealing, the non-Laves secondary phases were substantially suppressed as reported before [49,57]. The annealing increases the abundance of dominating phase (C14 in #177 and C15 in #193), which agrees with the previous work reported by Zhang et al [50]. The new finding is that for an alloy with about equal C14/C15 abundances (#190), the annealing does not change the phase abundance ratio. This alloy (#190) is very important in setting the baseline for the study of annealing effects due to the elimination of non-Laves secondary phase but not the changes in the phase structure. The contribution of extra C14 and C15 can be distilled by comparing the characteristics before and after annealing #177 and #193 alloys, respectively, and stripping out the contribution from non-Laves secondary phase.

Due to the overlap of C15 and some of the C14 peaks, only the lattice parameters for C14 were calculated and are listed in Table 2. In all three compositions, both *a* and *c* decrease after annealing and consequently result in smaller volumes for both unit cell and hydrogen occupation site. This outcome is in agreement with study on C14/BCC mixed alloys [51]. The shrinkage of unit cell volume is in the order #177 ($0.2\,Å^3$) < #193 ($0.4\,Å^3$) < #190 ($0.5\,Å^3$). Lower hydrogen storage capacity of C14 phase is expected after annealing. The a/c aspect ratio remains the same for C14-dominating #177 and is identical to the ideal ratio ($\sqrt{3/8} = 0.6124$). The a/c aspect ratio increases from the ideal ratio for C14/C15-par #190 and decreases toward the ideal ratio for C15-dominating #193 after annealing. The crystallite size was estimated from the full-width at half the maximum of a few major XRD diffraction peaks by the Scherrer equation [67] and is listed in Table 2. In all cases, the size of the reflection domain increases as the result of annealing.

3.2. SEM/EDS structural analysis

The EDS mappings of Cr for the three alloys before annealing show the best contrasts among phases and are shown in Fig. 2. The microstructures of this series of as-received, arc-melt prepared samples were also studied by transmission electron microscopy and reported before in a two-part publication [68,69]. The formation of various phases can be summarized as (1) dendritic growth of hexagonal C14 Laves phase (area with the brightest contrast); (2) peritectic solidification of cubic C15 Laves phase (area with the gray contrast); and (3) formation of cubic B2 phase in the interdendritic regions (area with the darkest contrast). The B2 phase decomposes in the solid state into a complex multivariate plate-like structure containing Zr_7Ni_{10}-type, Zr_9Ni_{11}-type and martensitic phases. The transformations obey crystallographic orientation relationships between the high-temperature parent BCC phase and Zr–Ni-type intermetallics, and consequently lead to a complex multivariant structure of faceted domains. The areas of the phases in each alloy agree with the phase abundance calculation from XRD data. The brightest area with C14 structure decreases from alloy #177, through #190, to #193, but the phase solidification formation remains unchanged.

The composition in each phase for the as-received samples was calculated by averaging several EDS results and is listed in Table 1. The distribution of Sn is very uneven and is absent in the areas we performed the SEM/EDS study. Similar uneven distribution of Sn was reported on similar alloys without annealing [61]. The e/a values calculated from the compositions can be used to identify the phases: C14 phase has an e/a value close to the lower end of the threshold, and C15's e/a value is higher than the same threshold. The B/A stoichiometry of C14 phase is always above 2 (2.04–2.10) while that of C15 phase has a wider spread from 1.93 to 2.13. Deviations from the ideal stoichiometry of C14 and C15 Laves phases have been discussed before and agree with our findings here [70]. There is no major difference in the chemical composition between C14 and C15 phases in the same alloy (only slightly higher Ni and lower Cr contents can be found in C15 phase). However, B2 phase is certainly high in Ti and Ni and low in V, Cr, and Mn. The low solubility of these B-elements in the non-Laves secondary phase was reported before on a study of Zr_7Ni_{10} based alloys [66]. The B/A stoichiometric ratios of the B2 phase (1.31 and 1.40) are between that of Zr_9Ni_{11} (1.22) and Zr_7Ni_{10} (1.43).

The SEM backscattering images of the samples after annealing are shown in Fig. 3. The chemical compositions of the numbered areas were studied by EDS and are listed in Table 1. In the case of #177A, besides occasional high-Sn inclusions (Zr_2Ni_2Sn identified in Ref. [51]), the alloy is mainly C14-structured. The high-Sn phase does not appear in the XRD spectrum due to its low volume

Table 1

The design composition (in bold) and the compositions measured by EDS in atomic percentages. The corresponding areas are in Figs. 2 and 3.

Area #	Ti	Zr	V	Ni	Co	Cr	Mn	Al	Sn	B/A	*e*/*a*	Phase
177design	**12.0**	**21.5**	**10.0**	**40.2**	**1.5**	**8.5**	**5.6**	**0.4**	**0.3**	1.99	6.91	
177-C14	10.3	22.3	9.9	42.3	1.1	7.6	5.6	0.8	0.0	2.06	7.01	C14
177-C15	10.0	22.0	10.2	43.1	1.3	7.2	5.5	0.9	0.0	2.13	7.06	C15
177-B2	21.8	19.8	1.6	52.8	0.7	0.9	1.8	0.6	0.0	1.40	7.29	B2-Mixture
190design	**12.0**	**21.5**	**10.0**	**40.2**	**5.0**	**5.5**	**5.1**	**0.4**	**0.3**	1.99	7.01	
190-C14	11.6	21.3	11.1	38.4	5.1	5.6	5.5	1.5	0.0	2.04	6.94	C14
190-C15	13.1	21.0	8.4	42.2	4.6	4.4	4.6	1.7	0.0	1.93	7.06	C15
190-B2	25.5	17.7	1.7	47.6	3.6	0.9	1.8	1.2	0.0	1.31	7.12	B2-Mixture
193design	**12.0**	**21.5**	**10.0**	**40.2**	**8.0**	**3.5**	**4.1**	**0.4**	**0.3**	1.99	7.09	
193-C14	10.1	22.1	12.1	35.4	9.0	4.7	5.2	1.3	0.0	2.10	6.93	C14
193-C15	11.4	21.4	10.5	39.9	8.4	3.7	4.7	0.0	0.0	2.05	7.13	C15
193-B2	26.8	16.5	1.8	45.8	5.9	0.5	1.7	1.1	0.0	1.31	7.12	B2-Mixture
177A-1	4.5	36.0	0.8	39.5	0.4	0.7	1.3	0.4	16.5	1.47	5.79	Zr_2Ni_2Sn
177A-2	12.2	21.4	10.4	40.5	1.6	7.2	5.7	0.6	0.5	1.98	6.91	C14
177A-3	13.0	21.2	9.9	41.0	1.6	6.7	5.5	0.6	0.6	1.93	6.91	C14
190A-1	9.1	35.8	3.7	35.7	2.5	1.5	2.2	0.4	9.2	1.23	6.03	Zr_2Ni_2Sn
190A-2	10.8	27.2	10.5	35.5	5.0	5.1	5.0	0.5	0.4	1.63	6.72	C14
190A-3	11.7	26.9	9.3	37.7	4.8	4.2	4.5	0.5	0.4	1.59	6.79	C14
190A-4	32.2	14.8	1.3	44.2	4.9	0.4	1.6	0.4	0.2	1.13	6.95	B2-Mixture
193A-1	8.5	30.5	3.8	38.8	3.9	0.7	1.9	0.4	11.5	1.56	6.17	Zr_2Ni_2Sn
193A-2	10.7	21.9	11.5	39.8	8.5	2.3	4.3	0.5	0.4	2.06	7.08	C15
193A-3	11.9	21.5	10.3	41.1	8.3	1.9	4.0	0.6	0.4	1.99	7.12	C15
193A-4	32.2	11.5	2.3	41.3	9.7	0.2	1.7	0.6	0.5	1.29	7.04	B2-Mixture

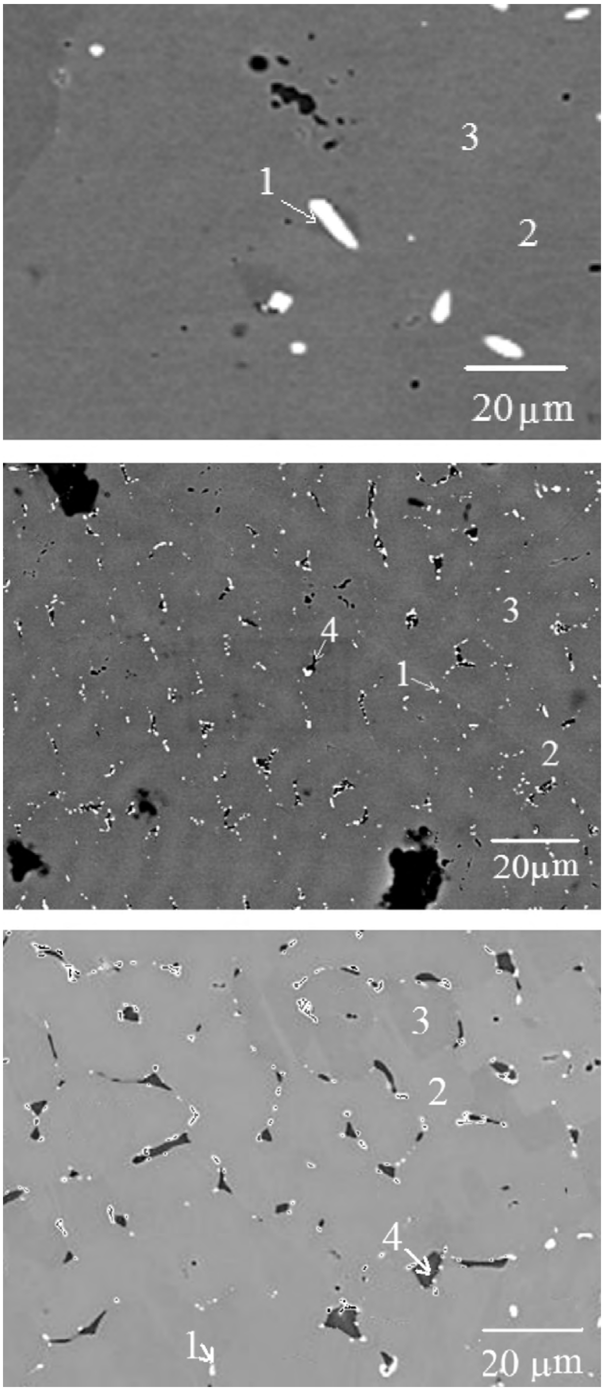

Fig. 3. SEM backscattering images for annealed #177 (a), #190 (b), and #193 (c). The compositions in the numbered areas were measured by EDS and the results are listed in Table 1.

fraction. Small variations in contrast are due to different crystallographic orientations. In the cases of #190A and #193A, some remaining B2-inclusions can be found. In the C14/C15-par #190A, the segregation of phases is larger than the current SEM scanning area (130 μm × 100 μm). Therefore, only one phase (in this case, C14) is seen from the micrograph. In general, results from SEM/EDS analysis agree with those from XRD analysis.

3.3. Gas phase study

Gas phase hydrogen storage properties of the alloys before and after annealing were studied by PCT. The resulting absorption and desorption isotherms measured at 30 °C are shown in Fig. 4. The information obtained from PCT study is summarized in Table 2. The maximum hydrogen storage at 30 °C of the alloy #190 reduces after annealing as consequence of shrinkage of storage site and elimination of catalytic non-Laves phase. The decrease of hydrogen storage in C14-predominating #177 and increase in C15-predominating #193 after annealing suggest that C15 phase may have better storage capacity as suggested by higher possible storage of C15 phase (4 H per AB_2 formula [11] vs. 3.4 H per AB_2 formula in C14 phase [71]). Comparing the reversible hydrogen storage of the same alloys before and after annealing, the C14-predominating #177A has the worst reversibility and the C15-predominating #193A has the best reversibility. Such results indicate that easier hydrogen release from the hydride of C15 structure. This assumption will be confirmed by the half-cell and diffusion measurements in the later section of this paper. The other possibility is that the remaining 0.4% of the non-Laves phase in #193A may assist in the reversibility of hydrogen storage. The desorption curve of #193A shows a typical two-component hydride material with close proximity, which was observed on some two-component vanadium-free AB_2 alloys before.

The mid-point pressure in the desorption isotherm is an indication of average metal-hydrogen bond strength. The changes in the mid-point pressures in alloys #177 and #190 after annealing are relatively small. It is because the change in phase abundance is small and overall average composition remains unchanged after annealing. Therefore, the average metal-hydrogen bond strength is not changed by annealing. The reduction in the mid-point pressure of #193 after annealing is due to the formation of a new hydride phase indicated by the second plateau in the desorption curve of #193A.

Slope factor (SF), as defined by the ratio of storage capacity in the absorption plateau region (between 0.01 and 0.5 MPa) to the total capacity, was used to quantify the inclination of the PCT curve. SF is a measurement of the uniformity of the alloy [72,73]. For the C14- and C15-predominated alloys, the SF increases (corresponding to a flatter isotherm) as the abundance of the major phase increases and consequently suggests that the alloy becomes more uniform, which is in agreement with the results from the annealing works done on $ZrV_{0.7}Mn_{0.5}Ni_{1.2}$ alloy [46]. For alloy #190, the abundances of C14 and C15 do not change much after annealing and therefore the SF remains almost unchanged.

3.4. Electrochemical measurement

Discharge capacities of the six alloys were measured in the flooded cell against the partially pre-charged $Ni(OH)_2$ as the positive electrode. Capacities measured at the slowest discharge rate (8 mA/g) for the first 10 cycles for each alloy are plotted in Fig. 5a. After 2–3 cycles, the full capacities stabilized and are listed in Table 3. The higher discharge capacity of #177 (401 mAh/g) is due to the lower e/a design. Higher e/a value has a stronger repelling force toward the extra electron brought in by the addition of hydrogen atom and thus weakens the hydrogen–metal bond strength. After annealing, similar losses in full storage capacity among the three compositions, independent of the phase component, are observed and can be linked to the shrinking of hydrogen occupation site. The HRD, defined as the ratio of the capacity measured at a fast rate (100 mA/g) to the total capacity, is plotted in Fig. 5b for the first 10 cycles of each alloy. The evolution of HRD in the first few cycles is related mainly to the pulverization rate of the alloy. The reduction in the initial pulverization in #190 after annealing can be attributed to the elimination of the non-Laves phase. The increases in the initial pulverization in #177 (C14-predominated) and #193 (C15-predominated) after annealing are due to their less ductile nature resulted by the larger grain size (seen from the SEM micrographs

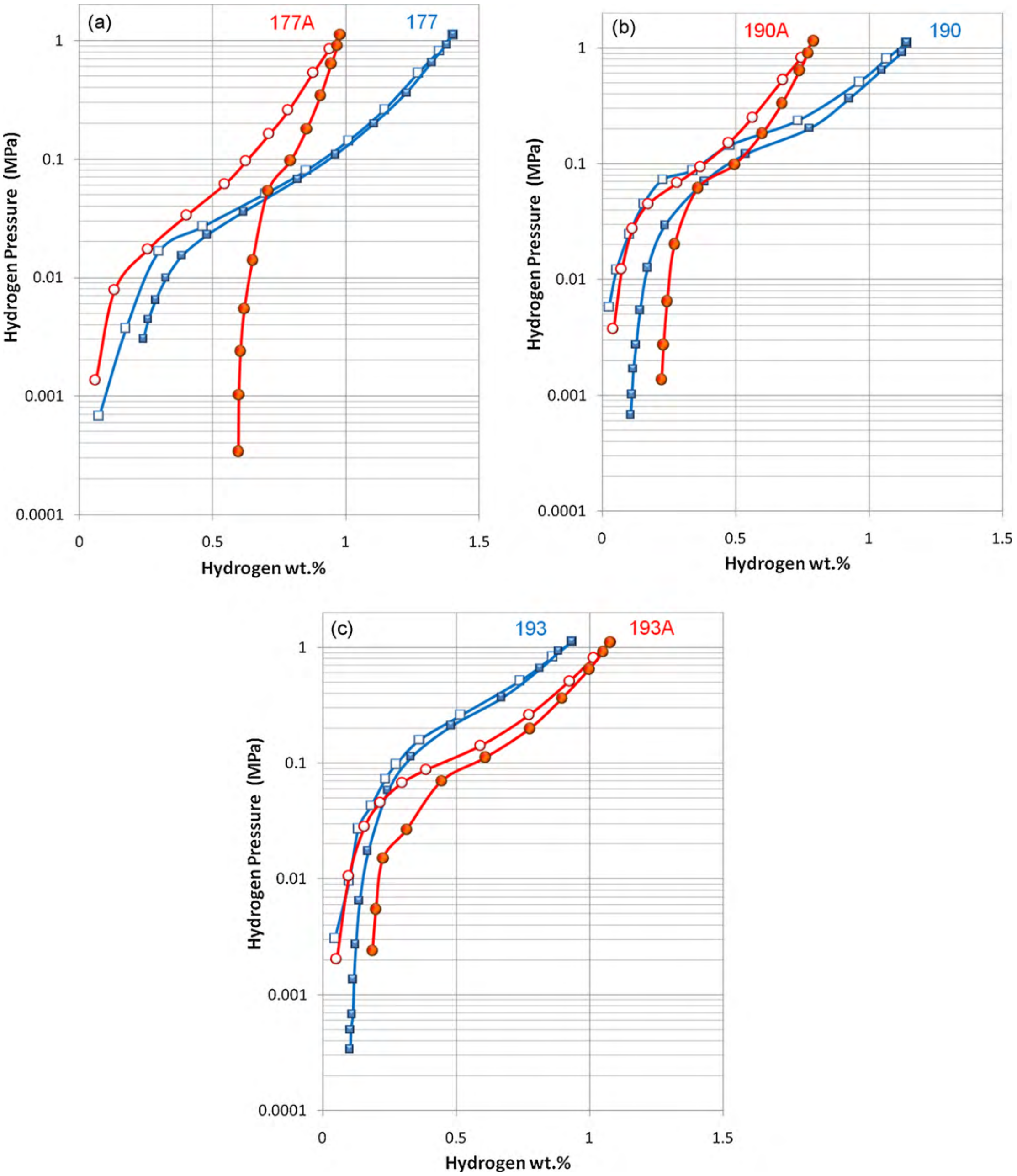

Fig. 4. 30 °C PCT isotherms of alloys #177 and #177A (a), #190 and #190A (b), and #193 and #193A. Open and solid symbols are for absorption and desorption curves, respectively.

in Fig. 3) and fewer grain boundaries. The HRD values at cycle 10 (HRD_{10}) are listed in Table 3. With the reduction in B2-precipitate, which is known to facilitate the Ni/MH battery activation process [27], the HRD_{10} of #190 decreases from 94% to 92% after annealing. The HRD_{10} of #177 remains the same while that of #193 increases from 90% to 94% after annealing. Therefore, increase in C15 phase abundance seems to correlate to the increase in HRD_{10} value, but not in the case of C14. This study suggests that C15 phase has a better HRD than C14 phase, which agrees with the observation from PCT analysis.

The HRD is further studied by the bulk diffusion coefficient (D) and the surface exchange current (I_o) measured and analyzed by a previously published method [74]. Both values for each alloy are listed in Table 3. In the case of bulk diffusion, the C15-predomited alloy is superior to the C14-predominated alloy, which can be attributed to two possible reasons: the higher density of stacking faults observed by transmission electron microscope [27] and higher hopping rate between hydrogen storage sites measured by quasielastic neutron scattering [75]. Marginal increases in D for #177 and #193 and substantial reduction in #190 are observed after annealing. The fine distribution of the non-Laves phase and the loss of the B2-precipitate [64,76,77] are the two causes for the decreased D value of #190A. The I_o values are similar for the three alloys before annealing, and all increase after annealing. There are two possible mechanisms to explain the increase in I_o by annealing. The first one is that the precipitation of Zr_2Ni_2Sn phase contributes to the increase in the surface reaction. With the largest number of Zr_2Ni_2Sn inclusion, #190A shows the highest I_o value. The second argument is that with the reduction in the Ni-rich B2 phase through annealing [46], the average Ni-content increases, which is known to be crucial to the surface reactivity [78,79]. In either case, the surface activity is more related to the chemical composition than

Table 2
Summary of XRD and gas phase storage properties of alloys in this study.

Alloy number	Phase abundance C14, %	Phase abundance C15, %	Phase abundance ZrNi$_x$,%	C14 lattice constant a, Å	C14 lattice constant c, Å	a/c aspect ratio	C14 unit cell volume, Å^3	C15 lattice constant a, Å	C15 unit cell volume, Å^3	XRD crystallite Size, Å	Max H-storage at 30 °C, %	Reversible H-storage at 30 °C, %	Mid-point pressure at 30 °C Des., MPa	30 °C PCT slope factor
177	71	26	4	4.9771	8.1288	0.6123	174.4			551	1.40	1.16	0.066	0.79
190	53	46	1	4.9647	8.1072	0.6124	173.1			530	1.14	1.01	0.16	0.81
193	32	67	1	4.9621	8.0977	0.6128	172.7	7.015	345.2	795	0.93	0.81	0.24	0.74
177A	94	6	0	4.9757	8.1266	0.6123	174.2			>1000	0.98	0.38	0.097	0.83
190A	57	43	0	4.9625	8.0941	0.6131	172.6			>1000	0.79	0.56	0.098	0.82
193A	7	93	0	4.9578	8.0962	0.6124	172.3	7.011	344.7	>1000	1.08	0.89	0.13	0.84

Table 3
Summary of electrochemical properties of alloys in this study.

Alloy number	Full capacity, mAh/g	High-rate dischargeability at cycle 10, %	Diffusion coefficient (D), $\times 10^{-10}$ cm^2/s	Exchange current (I_o), mA/g	Precharge, mAh/g	70% cycle life	30 Days charge retention, %	Specific power, W/kg	Low temp, %
177	401	89	5.6	25.8	17	615	40	155	85
190	360	94	11.1	28.7	21	675	31	200	93
193	335	90	12.1	24.3	28	545	25	130	86
177A	377	89	6.5	36.3	3	450	28	160	78
190A	344	92	7.4	44.9	0	365	13	108	93
193A	307	94	13.9	31.1	1	260	10	175	95

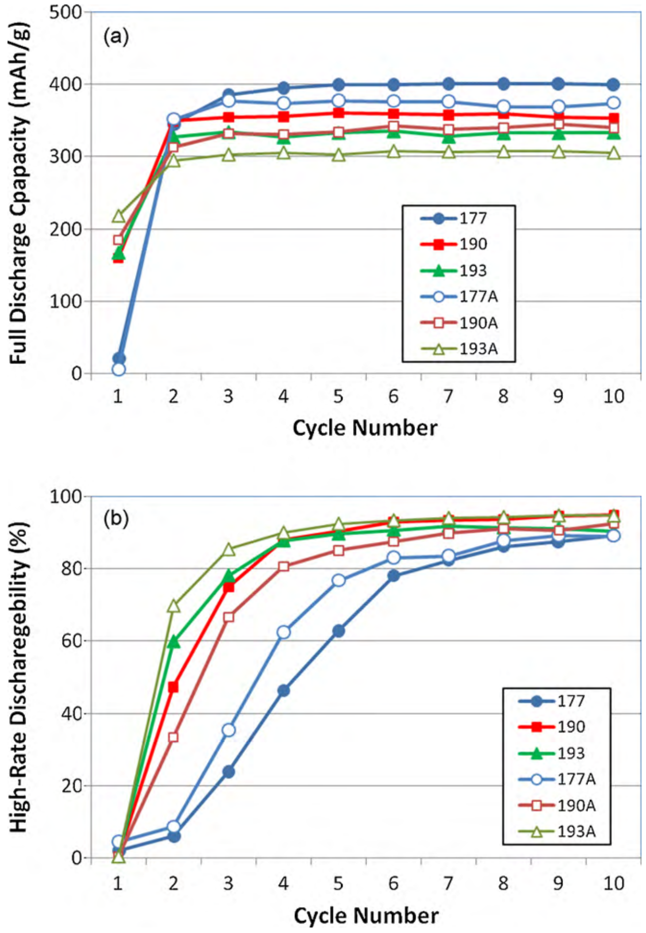

Fig. 5. The full discharge capacity (a) and high-rate dischargeability (b), as functions of formation cycle for all alloys in this study.

to the crystal structure. Therefore, the better HRD performance of C15 structure is due to its higher diffusion rate of hydrogen in the bulk. In the case of C14-predominating #177 alloy, although the surface exchange current increases by 40%, the HRD remains the same with a smaller increase in the diffusion coefficient. This is another proof that bulk diffusion plays more important role in the HRD. In this experiment, HRD is done in the flooded-cell configuration, there are other factors causing the no change in HRD of #177 after annealing. The specific power measured in a sealed cell configuration shows a small increase in alloy #177 after annealing corresponding to the higher *D* value.

Four kilograms of alloys were prepared by induction melt. Half of the ingot was annealed under the same condition as the arc-melt prepared sample. The composition and structure were verified to be the same as the arc-melt sample by ICP and XRD analyses. Electrode and sealed cell were fabricated as reported before [33]. The initial discharge capacity before any charge was from the hydrogen generated during the metal oxidation by the alkaline solution in the activation bath, and it can be used to quantify the ease of activation [80]. A higher initial discharge capacity can be correlated to an easier oxidation/activation of the alloy. The amount of precharge in mAh/g for each alloy is listed in Table 3. The precharge capacity increases as the Cr content in the alloy decreases. Cr is known to increase the surface resistance to alkaline solution [77,81–90]. After annealing, minimal precharge was observed in any alloy, which raises a major shortcoming of annealing: it makes the activation tougher than before annealing. There are two mechanisms related to the decrease in precharge capacity after annealing: the elimination of high Ti-content B2 phase, which is believed to facilitate the Ni/MH battery formation [27,34,91,55], and the decrease in the grain boundary density, as pointed out before a crucial parameter to the pulverization rate [92]. In both cases, the activation is less sensitive to the choice of main Laves phase in the alloy.

Four important Ni/MH technical parameters (cycle life, charge retention, specific power, and low temperature performance) for metal hydride electrode made from each alloy are listed in Table 3. For the cycle life reaching 70% of the original capacity, all three compositions degraded after annealing, which are opposite to the results from AB_5 alloys. One possible explanation for the mechanism causing this degradation in cycle life by annealing is that the equiaxial grain has a poorer cycle life than the dendrite-shape grain [93]. Dendrite-shape grain before annealing has a higher grain boundary density and is more difficult to pulverized, and thus contributes to a longer cycle life. The C15 phase with relatively higher Ni-content is assumed to carry a better cycle life due to the increase in ductility. However, the C15-predomianted #193 has the worst cycle life before annealing, and it became even worse after annealing. The reason may be that the higher hydrogen storage capability of C15 causes large lattice expansion and thus higher pulverization rate and lower cycle life.

Cr is known to improve the charge retention of AB_2 alloy by increasing the corrosion resistance to alkaline electrolyte [22,33,94]. As a result, the 30-day charge retentions of the alloys before annealing follow the order of the Cr content. The order remained unchanged but the value deteriorated after annealing. From the comparison, there is no clear correlation between the charge retention and the crystal structure of the main phase in the alloy. The degradation in charge retention by annealing may be connected to the formation of Zr_2Ni_2Sn phase and/or the reduction in grain boundary density. A detail study of the corrosion behavior of Zr_2Ni_2Sn phase is necessary to identify the cause for the degradation in charge retention by annealing.

The specific power of #190 dropped down to half after annealing due to the same reason in the reduced HRD value–reduction in the non-Laves phase. While the specific power of C14-predominated #177 remains about the same after annealing, in the specific power of the C15-predominated #193 increases as the C15 phase abundance increases after annealing. While increasing the majority phase abundance in the alloy by annealing improves the specific power in both C14 and C15 cases, the specific power from a C15-predominating #193A is higher than that from the C14-predominating #177A. Therefore, aside from the proximity effect from B2-related secondary phases, C15 phase appears to be higher in specific power.

The low temperature performance (ratio of the capacity measured at 0.5 C rate and $-10\,^{\circ}$C to the capacity measured at the same rate and room temperature) is originally believed to be related only to the surface area and surface reactivity [95]. By comparing the data in Table 3, a clear correlation can be established. As the amount of C14 phase increases, the low temperature performance deteriorates. However, the increase in C15 phase has a positive effect on the low temperature performance. Therefore, it seems that low temperature performance is also structure-related and C15 is a better choice for the low temperature application.

4. Summary

Three compositions with different *e*/*a* were designed to fabricate alloys with different C14/C15 ratios. After annealing, the abundance of the dominating phase (either C14 or C15) increases, the B2-precipitate is much reduced, and a new Zr_2Ni_2Sn phase is created. In the case of almost equal amount of C14/C15, the annealing does not change the C14/C15 ratio. By comparing the results obtained from samples before and after annealing, we conclude the following:

1. Annealing in AB_2 alloy reduces the lattice constants, cell volume, hydrogen storage capacity, electrochemical discharge capacity, HRD, diffusion constant, charge retention, cycle life, specific power, and makes activation harder.
2. In the gas phase, C15 structure offers higher hydrogen storage capacity and higher reversibility.
3. In electrochemical testing, the C15 structure offers better HRD, hydrogen bulk diffusion, specific power, and low temperature performance with a shortcoming of an inferior cycle life.

References

[1] I. Saldan, J. Frenzel, O. Shekhah, R. Chelmowski, A. Birkner, C. Wöll, J. Alloys Compd. 470 (2009) 568.
[2] S. Qiu, H. Chu, Y. Zhang, D. Sun, X. Song, L. Sun, F. Xu, J. Alloys Compd. 471 (2009) 453.
[3] M. Shibuya, J. Nakamura, H. Enoki, E. Akiba, J. Alloys Compd. 475 (2009) 543.
[4] M. Gao, H. Miao, Y. Zhao, Y. Liu, H. Pan, J. Alloys Compd. 484 (2009) 249.
[5] K. Young, M.A. Fetcenko, F. Li, T. Ouchi, J. Koch, J. Alloys Compd. 468 (2009) 482.
[6] K. Young, M.A. Fetcenko, T. Ouchi, F. Li, J. Koch, J. Alloys Compd. 469 (2009) 406.
[7] K. Young, T. Ouchi, J. Koch, M.A. Fetcenko, J. Alloys Compd. 477 (2009) 749.
[8] K. Young, T. Ouchi, W. Mays, B. Reichman, M.A. Fetcenko, J. Alloys Compd. 480 (2009) 434.
[9] K. Young, T. Ouchi, B. Reichman, W. Mays, R. Regmi, G. Lawes, M.A. Fetcenko, A. Wu, J. Alloys Compd. 489 (2010) 202.
[10] K. Young, R. Regmi, G. Lawes, T. Ouchi, B. Reichman, M.A. Fetcenko, A. Wu, J. Alloys Compd. 490 (2010) 282.
[11] D. Shaltiel, I. Jacob, D. Davidov, J. Less-Common Met. 53 (1977) 117.
[12] I. Jacob, D. Shaltiel, J. Less-Common Met. 65 (1979) 117.
[13] D.P. Shoemaker, C.B. Shoemaker, J. Less-Common Met. 68 (1979) 43.
[14] C.B. Magee, J. Liu, C.E. Lundin, J. Less-Common Met. 78 (1981) 119.
[15] A.F. Andresen, J. Less-Common Met. 88 (1982) 1.
[16] D.G. Westlake, J. Less-Common Met. 90 (1983) 251.
[17] D. Ivey, D. Northwood, J. Less-Common Met. 115 (1986) 23.
[18] D. Ivey, D. Northwood, Z. Phys. Chem. Neue Folge Bd. 147S (1986) 191.
[19] S. Asano, S. Ishida, J. Magn. Magn. Mater. 70 (1987) 39.
[20] Y. Moriwaki, T. Gamo, A. Shintani, T. Iwaki, Denki Kagaku 57 (1989) 488.
[21] S. Wakao, H. Sawa, Denki Kagaku 59 (1991) 950.
[22] S.R. Ovshinsky, M.A. Fetcenko, J. Ross, Science 260 (1993) 176.
[23] J.Y. Yu, Y.Q. Lei, C.P. Chen, J. Wu, Q.D. Wang, J. Alloys Compd. 231 (1995) 578.
[24] K.H. Young, M.A. Fetcenko, S.R. Ovshinsky, T. Ouchi, B. Reichman, W.C. Mays, Hydrogen at surface and interfaces, in: G. Jerkiewicz, J.M. Feliu, B.N. Popov (Eds.), Electrochemical Society Proceeding, vol. 2000–16, 2000, p. 60.
[25] F. Stein, M. Palm, G. Sauthoff, Intermetallics 12 (2004) 713.
[26] F. Stein, M. Palm, G. Sauthoff, Intermetallics 13 (2005) 1056.
[27] X. Song, X. Zhang, Y. Lei, Z. Zhang, Q. Wang, Int. J. Hydrogen Energy 24 (1999) 455–459.
[28] X.G. Yang, W.K. Zhang, Y.Q. Lei, Q.D. Wang, J. Electrochem. Soc. 146 (1999) 1245.
[29] Y.L. Du, X.G. Yang, Y.Q. Lei, M.S. Zhang, Int. J. Hydrogen Energy 27 (2002) 695.
[30] J. Huot, E. Akiba, T. Ogura, Y. Ishido, J. Alloys Compd. 218 (1995) 101.
[31] C. Iwakura, H. Kasuga, I. Kim, H. Inoue, M. Matsuoka, Electrochim. Acta 41 (1996) 2691.
[32] J. Chen, S.X. Dou, H.K. Liu, J. Alloys Compd. 256 (1997) 40.
[33] K. Young, T. Ouchi, M.A. Fetcenko, J. Alloys Compd. 476 (2009) 774.
[34] Q.A. Zhang, Y.Q. Lei, X.G. Yang, K. Ren, Q.D. Wang, J. Alloys Compd. 292 (1999) 241.
[35] Y.L. Du, X.G. Yang, Q.A. Zhang, Y.Q. Leo, M.S. Zhang, Int. J. Hydrogen Energy 26 (2001) 333.
[36] G.L. Lü, K.Y. Shu, L.S. Chen, X.Y. Song, X.G. Yang, Y.Q. Lei, Q.D. Wang, J. Alloys Compd. 293–295 (1999) 107.
[37] L. Chen, F. Wu, M. Tong, D.M. Chen, R.B. Long, Z.Q. Shang, H. Liu, W.S. Sun, K. Wang, L.B. Wang, Y.Y. Li, J. Alloys Compd. 293–295 (1999) 508.
[38] K. Shu, Y. Lei, X. Yang, G. Lin, Q. Wang, G. Lü, L. Chen, J. Alloys Compd. 293–295 (1999) 756.
[39] S.K. Zhang, Q.D. Wang, Y.Q. Lei, G.L. Lü, L.X. Chen, F. Wu, J. Alloys Compd. 330–332 (2002) 855.
[40] S.K. Zhang, K.Y. Shu, Y.Q. Lei, G.L. Lü, Q.D. Wang, J. Alloys Compd. 352 (2003) 158.
[41] Y. Zhang, P. Li, X. Wang, Y. Lin, X. Qu, J. Alloys Compd. 364 (2004) 289.
[42] Y. Zhu, H. Pan, Y. Liu, R. Li, Q. Jin, Q. Wang, Rare Metal Mater. Eng. 3 (2004) 262.
[43] Y. Zhang, P. Li, X. Wang, Y. Qi, Y. Lin, G. Wang, Rare Metal Mater. Eng. 33 (2004) 1321.
[44] H. Liu, J. Bai, R. Zhang, B. Hou, Mach. Des. Manuf. 6 (2004) 91.
[45] K. Young, J. Koch, T. Ouchi, A. Banik, M.A. Fetcenko, J. Alloys Compd. 496 (2010) 669.
[46] S. Lee, S. Kim, J. Yu, K. Jang, J. Lee, J. Electrochem. Soc. 145 (1998) 1953.
[47] H.J. Chuang, S.S. Huang, C.Y. Ma, S.L.I. Chan, J. Alloys Compd. 285 (1999) 284.
[48] S. Lee, J. Yu, H. Lee, K. Jang, J. Lee, J. Alloys Compd. 293–295 (1999) 601.
[49] W.K. Zhang, C.A. Ma, X.G. Yang, Y.Q. lei, Q.D. Wang, G.L. Lu, J. Alloys Compd. 293–295 (1999) 691.
[50] Q.A. Zhang, Y.Q. Lei, X.G. Yang, K. Ren, Q.D. Wang, J. Alloys Compd. 292 (1999) 236.
[51] Q.A. Zhang, Q. Lei, X.G. Yang, Y.L. Du, Q.D. Wang, J. Alloys Compd. 305 (2000) 125.
[52] Z. Shi, S. Chumbley, F.C. Laabs, J. Alloys Compd. 312 (2000) 41.
[53] M. Bououdina, C. Lenain, L. Aymard, J.L. Soubeyroux, D. Fruchart, J. Alloys Compd. 327 (2001) 178.
[54] Y. Zhu, H. Pan, M. Gao, Y. Liu, Q. Wang, J. Alloys Compd. 347 (2002) 279.
[55] Q.A. Zhang, Y.Q. Lei, J. Alloys Compd. 368 (2004) 362.
[56] Y. Makihara, Y. Iwata, K. Umeda, Y. Miyairi, H. Fujii, Mater. Res. Soc. Symp. Proc. 927 (2006) 1.
[57] A. Visintin, H.A. Peretti, F. Ruiz, H.L. Corso, W.E. Triaca, J. Alloys Compd. 428 (2007) 244.
[58] H. Liu, R. Li, Foundry Technol. 28 (2007) 179.
[59] K. Young, T. Ouchi, A. Banik. J. Koch, M.A. Fetcenko, J. Alloys Compd. (unpublished).
[60] K. Young, M.A. Fetcenko, T. Ouchi, F. Li, J. Koch, J. Alloys Compd. 464 (2008) 238.
[61] K. Young, M.A. Fetcenko, J. Koch, K. Morii, T. Shimizu, J. Alloys Compd. 486 (2009) 559.
[62] J.H. Zhu, P.K. Liaw, C.T. Liu, Mater. Sci. Eng. A239/A240 (1997) 260.
[63] J.H. Zhu, C.T. Liu, P.K. Liaw, Intermetallics 7 (1999) 1011.
[64] B.S. Chao, R.C. Young, S.R. Ovshinsky, D.A. Pawlik, B. Huang, J.S. Im, B.C. Chakoumakos, New materials for batteries and fuel, in: D. Doughty, L. Nazar, M. Arakawa, H.-P. Brack, K. Naoi (Eds.), Materials Research Sociaty Symposium Proceedings, Vol. 575, Warrendale, PA, 1999, p. 193.
[65] S. Amerioun, T. Yokosawa, S. Lidin, U. Häussermann, Inorg. Chem. 43 (2004) 4751.
[66] K. Young, T. Ouchi, B. Huang, J. Nei, M.A. Fetcenko, J. Alloys Compd. 501 (2010) 236.
[67] H.P. Klug, L.E. Alexander, X-ray Diffraction Procedures for Polycrystalline and Amorphous Materials, 2nd ed., John Wiley & Sons, New York, 1974, p. 656.
[68] W.J. Boettinger, D.E. Newbury, K. Wang, L.A. Bendersky, C. Chiu, U.R. Kattner, K. Young, B. Chao, Metall. Mater. Trans. A (2010), doi:10.1007/s11661-010-0237-z.
[69] L.A. Bendersky, K. Wang, W.J. Boettinger, D.E. Newbury, K. Young, B. Chao, Metall. Mater. Trans. A (2010), doi:10.1007/s11661-010r-r0240-4.
[70] D.J. Thoma, J.H. Perepezko, J. Alloys Compd. 224 (1995) 330.
[71] A. Pebler, E.A. Gulbransen, Electrochem. Technol. 4 (1966) 211.
[72] C.N. Park, S. Luo, T.B. Flanagan, J. Alloys Compd. 384 (2004) 203.
[73] S. Luo, C.N. Park, T.B. Flanagan, J. Alloys Compd. 384 (2004) 208.
[74] F. Li, K. Young, T. Ouchi, M.A. Fetcenko, J. Alloys Compd. 471 (2009) 371.
[75] A.V. Skripov, M. Pionke, O. Randl, R. Hempelmann, J. Phys.: Condens. Matter 11 (1999) 1489.
[76] J.M. Joubert, M. Latroche, A. Percheron-Guégan, J. Alloys Compd. 231 (1995) 494.
[77] J.M. Joubert, M. Latroche, A. Percheron-Guégan, J. Bouet, J. Alloys Compd. 240 (1996) 219.
[78] K. Young, B. Huang, R.K. Regmi, G. Lawes, Y. Liu, J. Alloys Compd. (2010), doi:10.1016/j.jallcom.2010.07.086.
[79] K. Young, T. Ouchi, Y. Liu, B. Reichman, W. Mays, M.A. Fetcenko, J. Alloys Compd. 480 (2009) 521.
[80] C. Iwakura, W.K. Choi, S. Zhang, H. Inoue, Electrochim. Acta 44 (1998) 1677.
[81] Y. Moriwaki, T. Gamo, H. Seri, T. Iwaki, J. Less-Common Met. 172–174 (1991) 1211.
[82] J.M. Park, J.-Y. Lee, J. Less-Common Met. 167 (1991) 245.
[83] A. Züttel, F. Meli, L. Schlapabach, Z. Phys. Chem., Bd. 183S (1994) 355.
[84] X.G. Yang, Y.Q. Lei, W.K. Zhang, G.M. Zhu, Q.D. Wang, J. Alloys Compd. 243 (1996) 151.
[85] B. Knosp, C. Jordy, Ph. Blanchard, T. Berlureau, J. Electrochem. Soc. 145 (1998) 1478.
[86] J.S. Yu, S.M. Lee, K. Cho, J.Y. Lee, J. Electrochem. Soc. 147 (2000) 2013.
[87] Y.F. Zhu, H.G. Pan, G.Y. Wang, M.X. Gao, J.X. Ma, C.P. Chen, Q.D. Wang, Int. J. Hydrogen Energy 26 (2001) 807.
[88] G.Y. Wang, Y.H. Xu, H.G. Pan, Q.D. Wang, Int. J. Hydrogen Energy 28 (2003) 499.
[89] H.A. Peretti, A. Visintin, L.V. Mogni, H.L. Corso, J. Andrade Gamboa, D. Serafini, W.E. Triaca, J. Alloys Compd. 354 (2003) 181.
[90] H. Pan, R. Li, M. Gao, Y. Liu, Q. Wang, J. Alloys Compd. 404–406 (2005) 669.
[91] A. Züttel, F. Meli, L. Schlapabach, J. Alloys Compd. 231 (1995) 645.
[92] M. Gao, S. Zhang, H. Miao, Y. Liu, H. Pan, J. Alloys Compd. 489 (2010) 552.
[93] K.Y. Shu, X.G. Yang, S.K. Zhang, G.L. Lu, Y.Q. Lei, Q.D. Wang, J. Alloys Compd. 306 (2000) 122.
[94] M.A. Fetcenko, S.R. Ovshinsky, K. Young, B. Reichman, C. Fierro, J. Koch, F. Martin, W. Mays, T. Ouchi, B. Sommers, A. Zallen, J. Alloys Compd. 330–332 (2002) 752.
[95] M.A. Fetcenko, S.R. Ovshinsky, B. Reichman, K. Young, C. Fierro, J. Koch, A. Zallen, W. Mays, T. Ouchi, J. Power Sources 165 (2007) 544.